SUPPLEMENTARY INFORMATION

Carbon microspheres with well-developed micro- and mesopores as excellent selenium host materials for lithium–selenium batteries with superior performances

Gi Dae Park[a], Jong Hwa Kim[b], Jung-Kul Lee*[c] and Yun Chan Kang*[a]

[a]*Department of Materials Science and Engineering, Korea University, Anam-Dong, Seongbuk-Gu, Seoul 136-713, Republic of Korea, E-mail: yckang@korea.ac.kr; Fax: (+82) 2-928-3584*

[b]*Daegu Center, Korea Basic Science Institute, 80 Daehakro Bukgu, Daegu 702-701, Republic of Korea*

[c]*Department of Chemical Engineering, Konkuk University, Hwayang-dong, Gwangjin-gu Seoul 143-701, Republic of Korea, E-mail: jkrhee@konkuk.ac.kr*

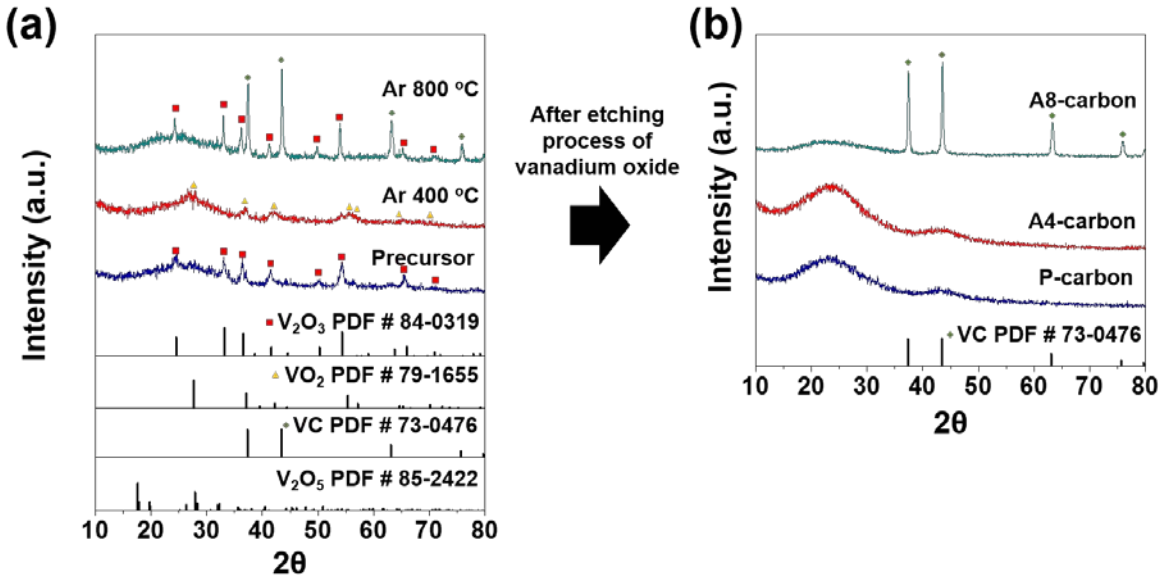

Fig. S1 (a) XRD patterns of as-synthesized precursor microspheres by spray pyrolysis and post-treated microspheres at 400, 800 °C and (b) XRD patterns of carbon (P-carbon, A4-carbon) and VC–C (A8-carbon) microspheres after etching process.

.

.

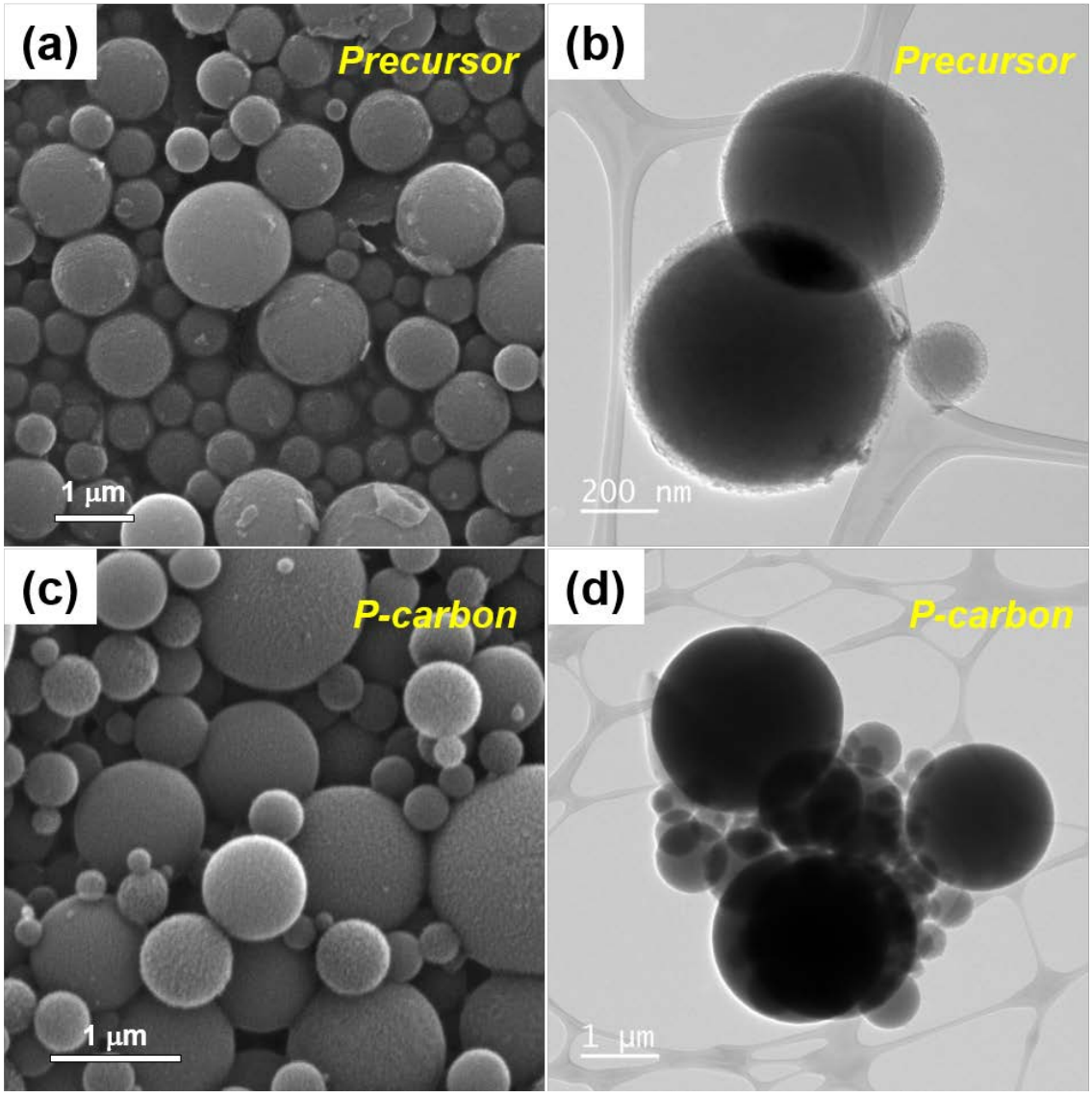

Fig. S2 Morphologies of as-synthesized precursor microspheres by spray pyrolysis (a,b) before and (c,d) after the etching process: (a) SEM, and (b) low-resolution TEM, (c) SEM, and (d) low-resolution TEM images.

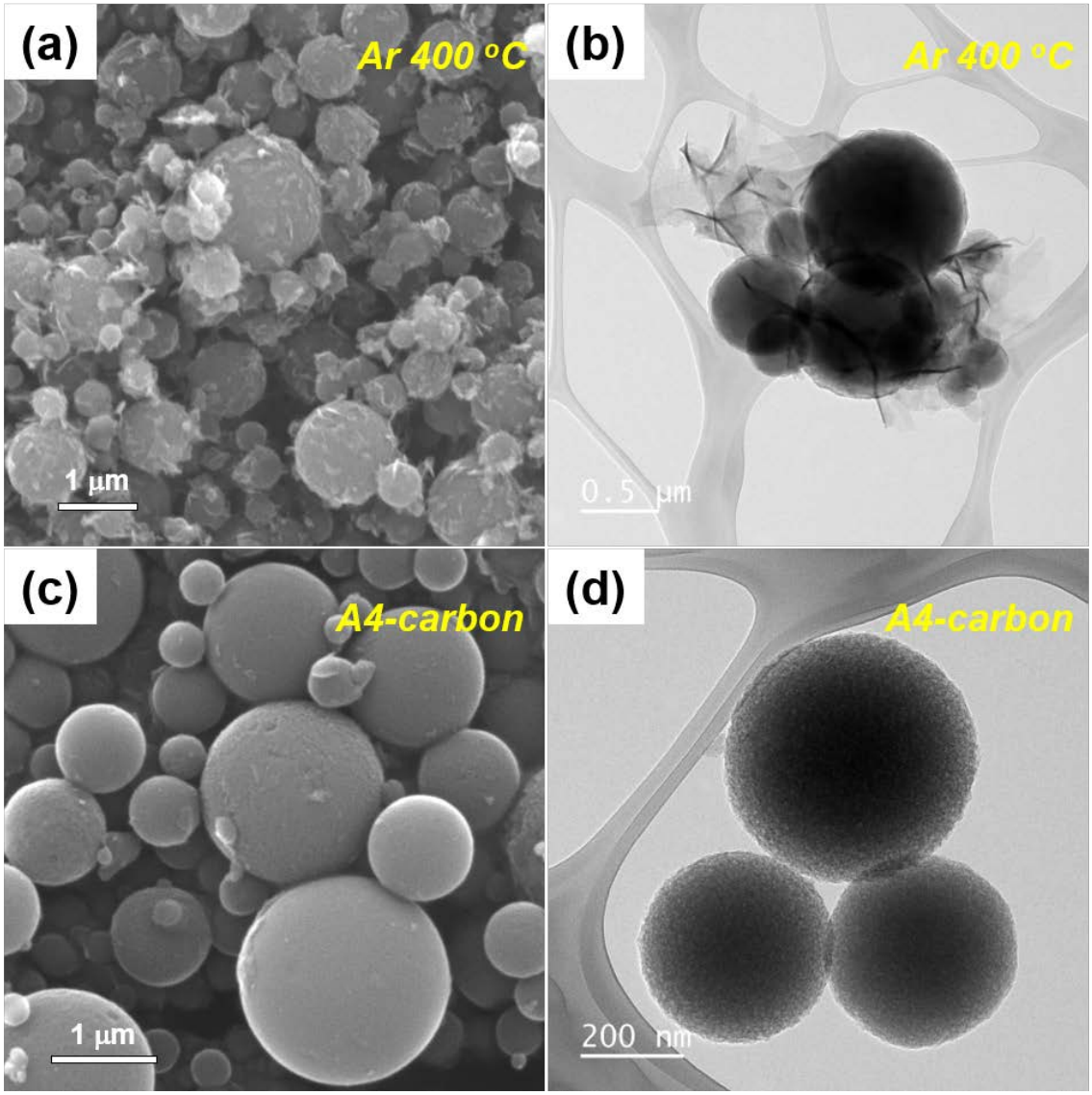

Fig. S3 Morphologies of post-treated microspheres at 400 °C (a,b) before and (c,d) after the etching process: (a) SEM and (b) low-resolution TEM, (c) SEM, and (d) low-resolution TEM images.

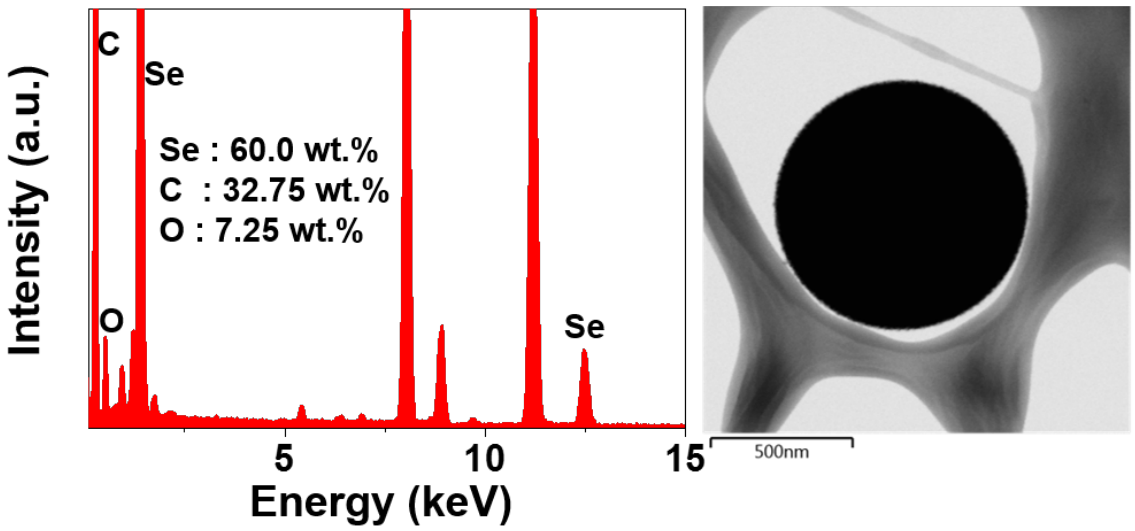

Fig. S4 Energy-dispersive X-ray (EDX) spectrum and TEM image of Se-loaded A4-carbon.

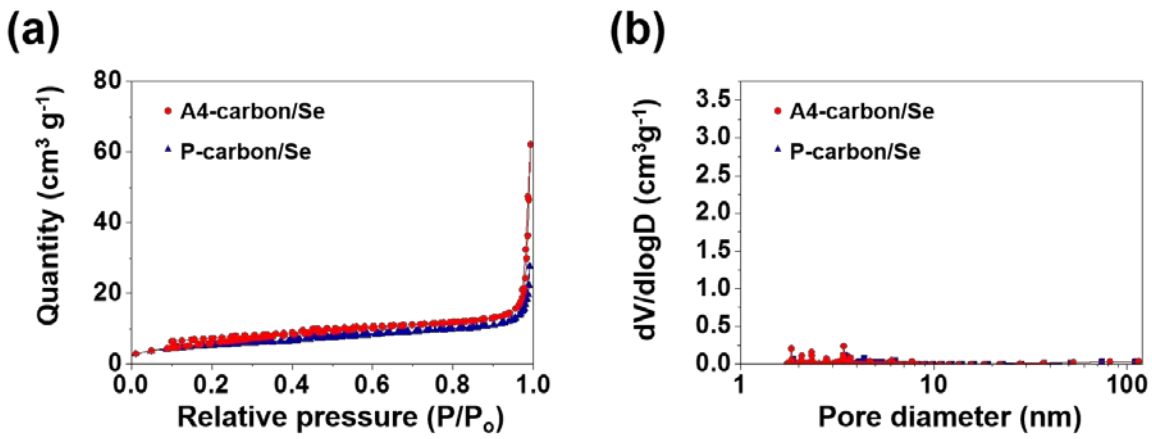

Fig. S5 (a) N_2 gas adsorption and desorption isotherms and (b) Barrett–Joyner–Halenda (BJH) pore size distributions of Se-loaded P- and A4-carbon.

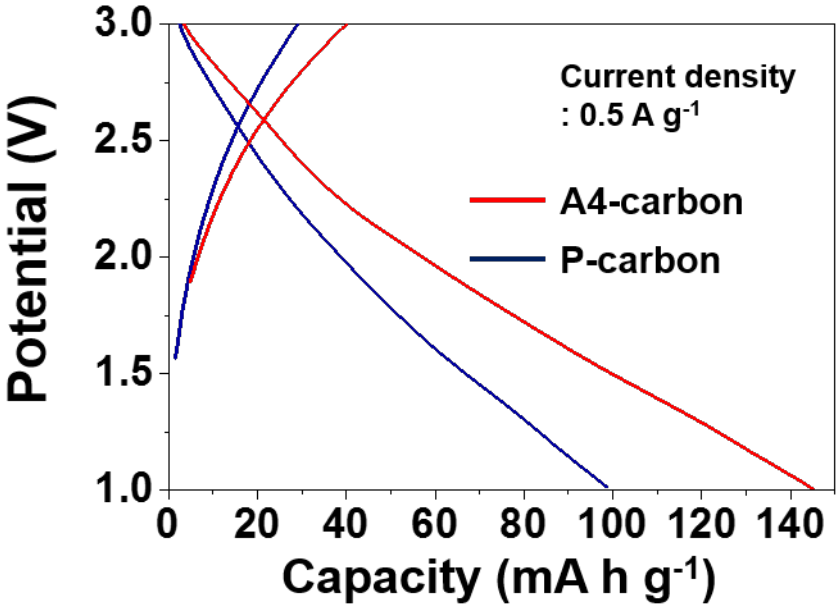

Fig. S6 Initial discharge and charge curves of P- and A4-carbon microspheres without Se at a current density of 0.5 A g^{-1}.

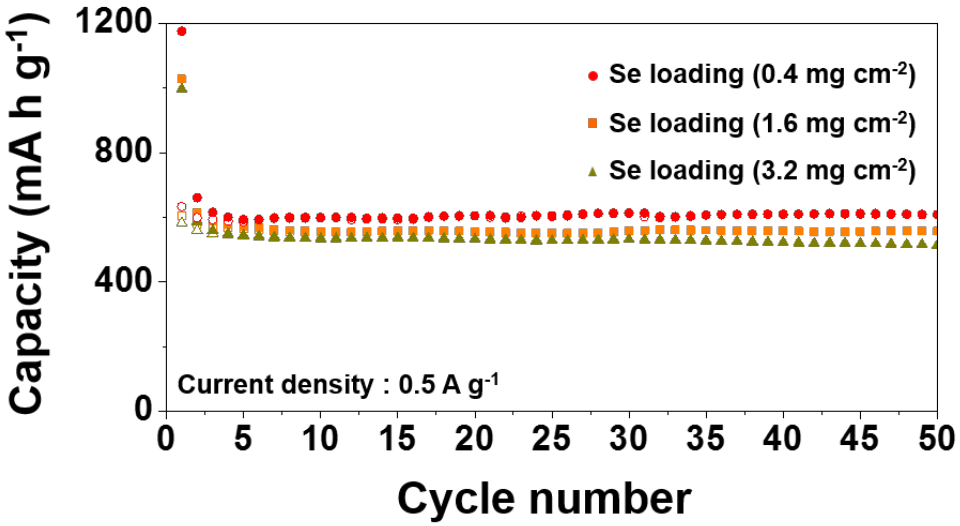

Fig. S7 Effect of loading rate of cathode material on cycling performance of Se-loaded A4-carbon electrode at a current density 0.5 A g^{-1}

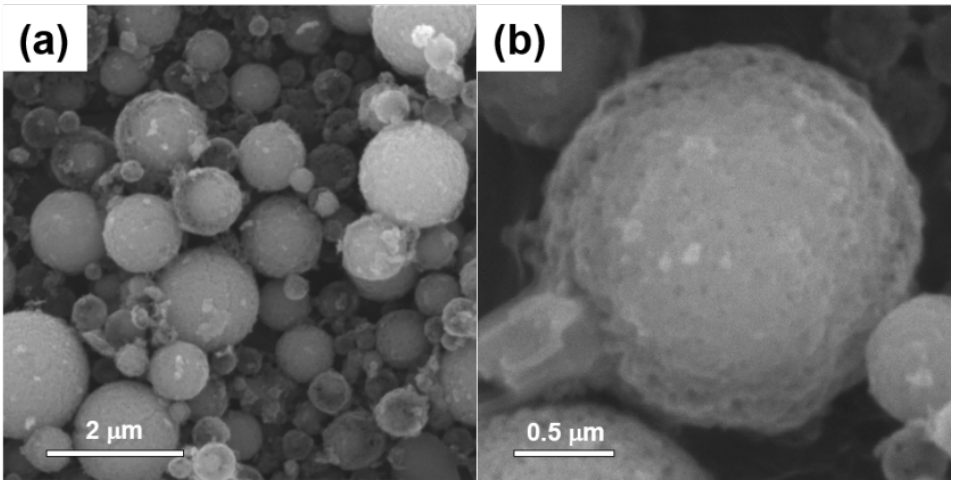

Fig. S8 Morphologies of Se-loaded A8-carbon microspheres.

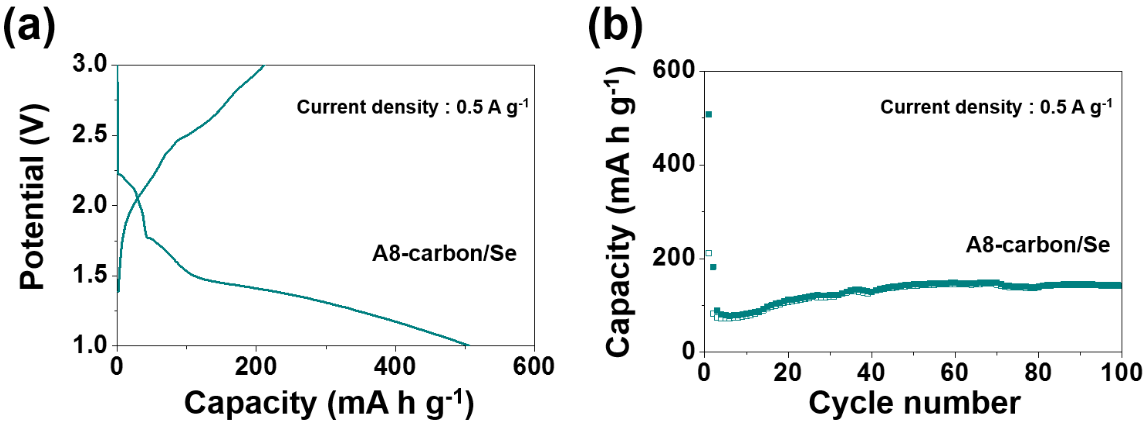

Fig. S9 Electrochemical properties of Se-loaded A8-carbon microspheres at a current density 0.5 A g^{-1}: (a) initial charge-discharge profile and (b) cycling performance.

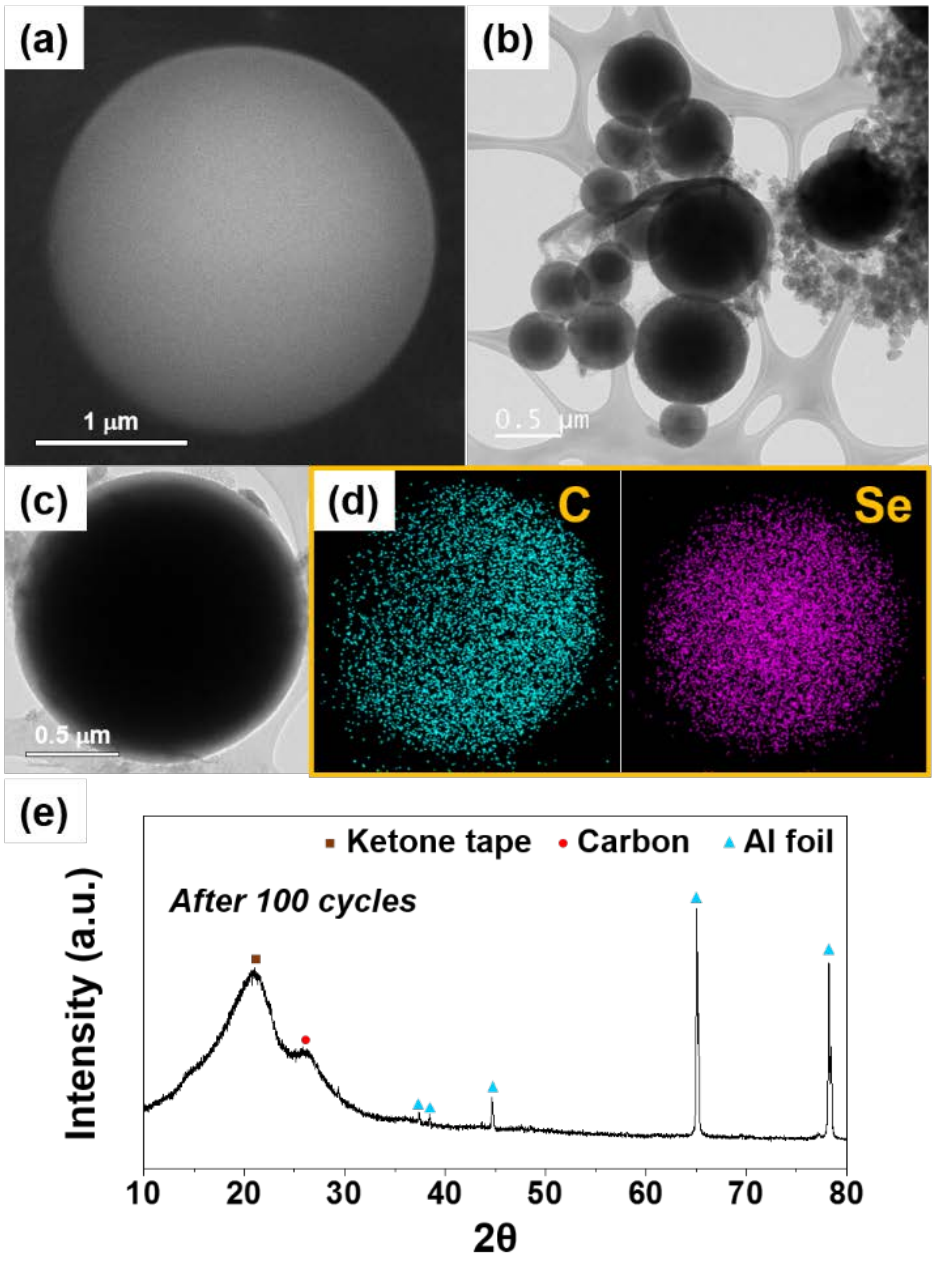

Fig. S10 Morphologies, elemetal mapping images, and XRD pattern of Se-loaded A4-carbon obtained at a fully charged state after 100 cycles: (a) SEM image, (b,c) TEM images, (d) elemental mapping images, and (e) XRD pattern.

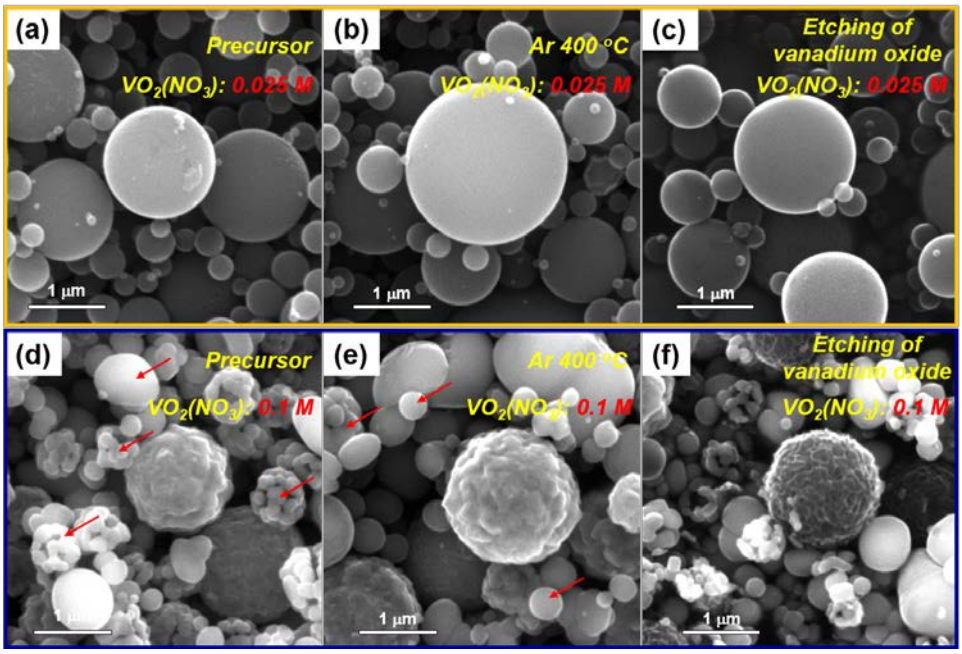

Fig. S11 Morphologies of (a,d) as-synthesized precursor microspheres by spray pyrolysis from the spray solution wih various concentrations of $VO_2(NO_3)$ and post-treated microspheres at 400 °C (b,e) before and (c,f) after etching process.

The effect of V/C ratio on the morphologies of carbon microspheres synthesized by spray pyrolysis and electrochemical properties of carbon/Se electrodes were studied. The concentration of $VO_2(NO_3)$ in spray solution influenced the morphologies of vanadium oxide-C composite microspheres as shown in Fig. S11, in which the concentration of sucrose in the spray solution was fixed at 0.1 M. The vanadium oxide-C composite prepared from the spray solution with 0.025 M $VO_2(NO_3)$ showed similar morphologies before and after post-treatment at 400 ^oC. VO_2 nanosheets were not observed in the SEM image of the post-treated microspheres in Fig. S11b. In addition, the morphologies (Fig. S11c) of carbon microspheres obtained after vanadium oxide etching process were similar to those of vanadium oxide-C composite. The vanadium oxide-C composite prepared from the spray solution with 0.1 M $VO_2(NO_3)$ shown in Fig. S11d had irregular morphologies. Vanadium oxide powders separated from the carbon matrix were observed in the SEM image as shown by arrows in Fig. S11d and e. In addition, etching of vanadium oxide powders were not well performed in the conditions applied in this study as shown in Fig. S11f

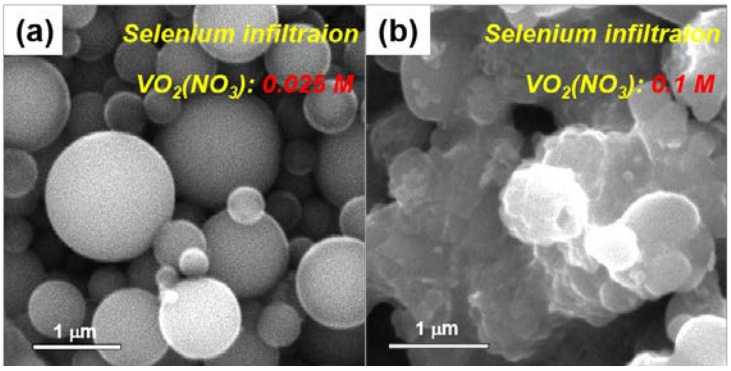

Fig. S12 Morphologies of the microspheres prepared from the spray solutions with (a) 0.025 and (b) 0.1 M $VO_2(NO_3)$ after Se infiltration.

The carbon microspheres obtained from the spray solutions with various concentrations of V source were applied as host material for Se-loading. The morphologies of Se-loaded carbon microspheres are shown in Fig. S12. The Se was well infiltrated into the carbon microspheres prepared from the spray solution with 0.025 M $VO_2(NO_3)$ as shown in Fig. S12a. However, melted Se was observed in the SEM image of the carbon microspheres prepared from the spray solution with 0.1 M $VO_2(NO_3)$ after Se infiltration as shown in Fig. S12a. The low pore volume owing to the existence of vanadium oxide powders resulted in low infiltration rate of Se into the microspheres.

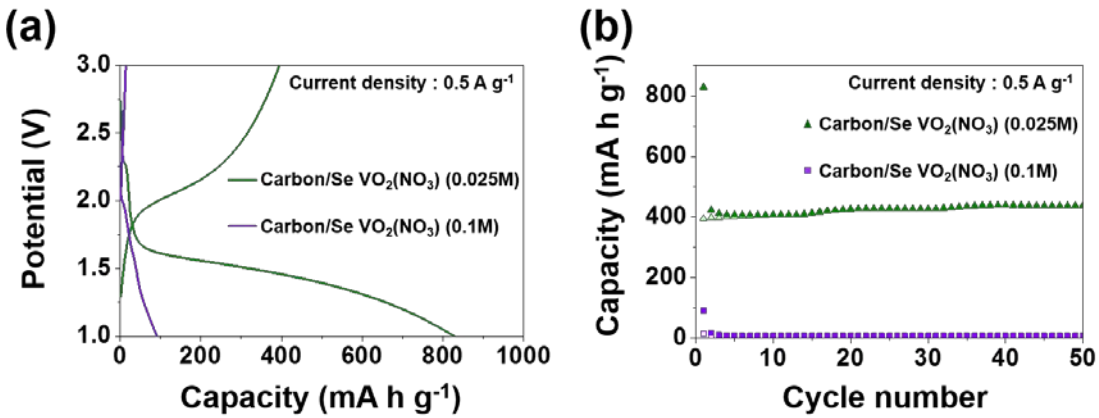

Fig. S13 (a) Initial discharge and charge curves and (b) cycling performances of the microspheres prepared from the spray solutions with 0.025 and 0.1 M $VO_2(NO_3)$ after Se infiltration.

The Se-loaded carbon microspheres shown in Fig. S13 showed lower capacities than those of the main sample shown in Fig. 7d. The low amount of vanadium oxide in the vanadium oxide-C composite microspheres did not improve the pore volume of mesopore in the carbon microspheres during the post-treatment at 400 ^{o}C. Therefore, carbon microspheres prepared from the spray solution with 0.025 M $VO_2(NO_3)$ showed low capacities for lithium-ion storage after Se-loading. On the other hand, loading of bulk Se into the vanadium oxide-carbon composite microspheres resulted in extremely low capacities in Fig. S13.

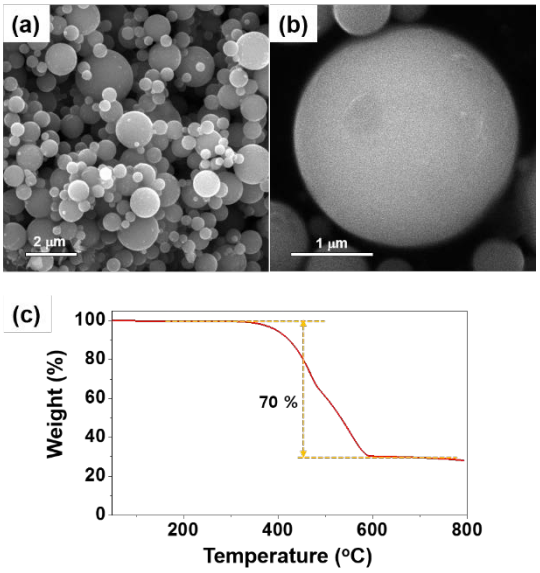

Fig. S14 (a,b) Morphologies and (c) TG curve of Se-loaded A4-carbon with a Se content of 70 wt%.

The morphologies and electrochemical properties of Se-loaded A4-carbon with a Se content of 70 wt% are shown in Fig. S14 and S15, respectively. The SEM images shown in Fig. S14a,b reveal that even though Se content was increased, Se is still well infiltrated into highly porous carbon microspheres. A 70 wt% loading amount of Se in A4-carbon microsphere was confirmed by TG curve shown in Fig. S14c.

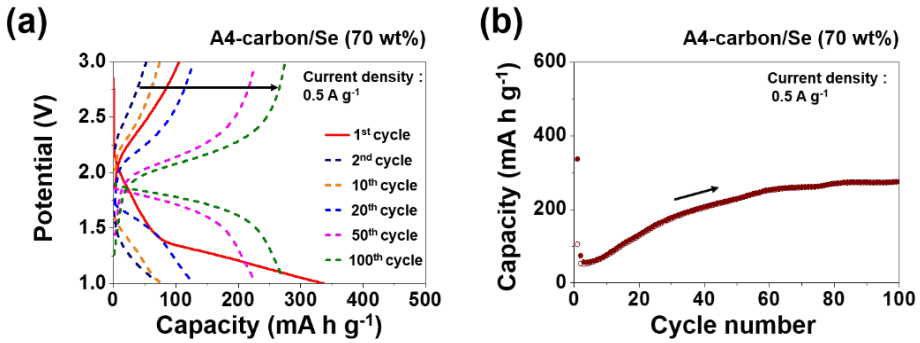

Fig. S15 Charge-discharge profiles at the 1st, 2nd, 10th, 20th, 50th, and 100th cycles, and cycling performance of Se-loaded A4-carbon with a Se content of 70 wt%: (a) charge-discharge profile, (b) cycling performance at current density of 0.5 A g^{-1}.

The charge-discharge profiles at the 1st, 2nd, 10th, 20th cycles of Se-loaded A4-carbon with a Se content of 70 wt% showed incomplete conversion reaction. However, after 50 cycles, distinct plateau which was related to transformation of chain-structured Se_n to Li_2Se was observed at 1.8 V. The cycling performance data also showed capacity increase as cycling proceeds as shown in Fig. S15b. Step-wise activation of Se-loaded A4-carbon increased the capacities during cycling. This result explained that liquid electrolyte was not well penetrated into carbon microspheres owing to full loading of Se into pores of A4-carbon microspheres. Also, the formation of nanochannels for penetration of the liquid electrolyte by partial structural damages of carbon microspheres during the repeated cycling enabled the conversion of Se_n located deep inside of carbon microspheres. Therefore, pore volume of microspheres should be increased to achieve the high amount Se-loaded carbon microspheres showing excellent lithium-ion storage performances. In the spray pyrolysis, pore volume of carbon microspheres could be increased by optimizing the preparation conditions, such as types of carbon source and inorganic additive materials, preparation temperature, etc

Table S1. Electrochemical properties of various Se-loaded carbon materials applied as lithium-selenium batteries reported in the previous literatures.

Materials	Current rate	Discharge capacity [mA h g^{-1}] and (cycle number)	Rate capacity [mA h g^{-1}] (current rate)	Ref
Se@mesoporous carbon composite	0.17 A g^{-1}	480 (1000)	229 (3.4 A g^{-1})	[S1]
Graphitic nanocarbon−selenium	0.34 A g^{-1}	376 (1000)	390 (6.8 A g^{-1})	[S2]
Se/micro–mesoporous carbon sphere	0.17 A g^{-1}	320 (500)	430 (3.4 A g^{-1})	[S3]
Flexible porous carbon nanofibers-selenium	0.5 A g^{-1}	516 (900)	306 (4.0 A g^{-1})	[S4]
Freestanding hollow double-shell Se@CNx nanobelts	0.8 A g^{-1}	453 (400)	474 (1.6 A g^{-1})	[S5]
Three-dimensional hierarchical graphene-CNT@Se	0.13 A g^{-1}	504 (150)	193 (6.8 A g^{-1})	[S6]
Se-nitrogen-doped carbon scaffolds	0.1 A g^{-1}	515 (50)	320 (2.0 A g^{-1})	[S7]
Polyaniline-coated selenium/carbon composites encapsulated in graphene	1.34 A g^{-1}	528 (500)	476 (3.4 A g^{-1})	[S8]
Selenium containing tube-in-tube carbon	0.34 A g^{-1}	301 (500)	190 (6.8 A g^{-1})	[S9]
Se/hierarchical porous carbon fiber composite	1.34 A g^{-1}	418 (1000)	408 (3.4 A g^{-1})	[S10]
Carbon microspheres with well-developed micro- and mesopores	**2.0 A g^{-1}**	**343 (2000)**	**265 (6.0 A g^{-1})**	**Our work**

References

[S1] C. Luo, Y. Xu, Y. Zhu, Y. Liu, S. Zheng, Y. Liu, A. Langrock and C. Wang, *ACS nano*, 2013, **7**, 8003-8010.

[S2] S.-F. Zhang, W.-P. Wang, S. Xin, H. Ye, Y.-X. Yin and Y.-G. Guo, *ACS Appl. Mater. Interfaces*, 2017, **9**, 8759-8765.

[S3] H. Ye, Y.-X. Yin, S.-F. Zhang and Y.-G. Guo, *J. Mater. Chem. A*, 2014, **2**, 13293-13298.

[S4] L. Zeng, W. Zeng, Y. Jiang, X. Wei, W. Li, C. Yang, Y. Zhu and Y. Yu, *Adv. Energy Mater.*, 2015, **5**, 1401377.

[S5] Q. Cai, Y. Li, Q. Li, J. Xu, B. Gao, X. Zhang, K. Huo and P. K. Chu, *Nano Energy*, 2017, **32**, 1-9.

[S6] J. He, Y. Chen, W. Lv, K. Wen, P. Li, Z. Wang, W. Zhang, W. Qin and W. He, *ACS Energy Lett.*, 2016, **1**, 16-20.

[S7] H. Lv, R. Chen, X. Wang, Y. Hu, Y. Wang, T. Chen, L. Ma, G. Zhu, J. Liang, Z. Tie, J. Liu, Z. Jin, *ACS Appl. Mater. Interfaces*, 2017, **9**, 25232-25238.

[S8] B. Wang, J. Zhang, Z. Xia, M. Fan, C. Lv, G. Tian, X. Li, *Nano Res.*, 2018, **11**, 2460-2469.

[S9] K. Balakumar, N. Kalaiselvi, *Carbon*, 2017, **112**, 79-90.

[S10] L. Zeng, X. Chen, R. Liu, L. Lin, C. Zheng, L. Xu, F. Luo, Q. Qian, Q. Chen, M. Wei, *J. Mater. Chem. A*, 2017, **5**, 22997-23005.